

Crystal nucleation for a model of globular proteins

Andrey Shirayev and James D. Gunton

Department of Physics, Lehigh University, Bethlehem, Pennsylvania 18015

(Received 9 September 2003; accepted 11 February 2004)

A continuum model of globular proteins proposed by Talanquer and Oxtoby [J. Chem. Phys. **109**, 223 (1998)] is investigated numerically, with particular emphasis on the region near the metastable fluid–fluid coexistence curve. Classical nucleation theory is shown to be invalid not only in the vicinity of the metastable critical point but also close to the liquidus line. An approximate analytic solution is also presented for the shape and properties of the nucleating crystal droplet. © 2004 American Institute of Physics. [DOI: 10.1063/1.1695321]

I. INTRODUCTION

In recent years there has been an enormous increase in the number of proteins that can be isolated, due to the rapid advances in biotechnology. However, the determination of the function of these proteins has been slowed by the difficulty of determining their crystal structure by standard x-ray crystallography. A major problem is that it is difficult to grow good quality protein crystals. Experiments have clearly shown that this crystallization depends sensitively on the physical factors of the initial solution of proteins. An important observation was made by George and Wilson,¹ who showed that x-ray quality globular protein crystals only result when the second virial coefficient, B_2 , of the osmotic pressure of the protein in solution lies within a narrow range. This corresponds to a rather narrow temperature window. For large positive B_2 , crystallization does not occur on observable time scales, whereas for large negative B_2 , amorphous precipitation occurs. Rosenbaum, Zamora, and Zukoski then showed² the crystallization of globular proteins could be explained as arising from attractive interactions whose range is small compared with the molecule's diameter (corresponding to the narrow window of B_2). In this case the gas–fluid coexistence curve is in a metastable region below the liquidus–solidus coexistence lines, terminating in a metastable critical point. In a seminal study, ten Wolde and Frenkel then showed³ in a simulation of a modified Lennard-Jones model with short range attractions that crystal nucleation is significantly enhanced in the vicinity of the metastable critical point, due to a reduction in the nucleation free energy barrier. Thus the conditions for optimal crystallization correspond to being near the metastable critical point. The reduction in the nucleation barrier results from the large density fluctuations that exist near the metastable critical point, which also affect the structure of the critical nucleus. Namely, the initial step toward formation of the critical droplet is the creation of a dense, liquidlike droplet which then forms a crystal nucleus in its interior. This process of first increasing the density and then forming a crystalline order is the opposite of what normally occurs in the liquid–solid phase transition at high temperatures and close

to the liquidus line. The authors also showed that classical nucleation theory is invalid in the vicinity of the critical point.

The idea that protein crystal nucleation could be enhanced by critical density fluctuations was subsequently reinforced in a density functional study by Talanquer and Oxtoby. They studied a phase field model with two order parameters, the local density $\rho(r)$ and a structural order parameter $m(r)$. The phenomenological free energy functional was assumed to have a van der Waals fluid branch and a van der Waals-type solid branch. Their numerical solution of the Euler–Lagrange equations for the nucleating critical droplet and free energy barrier confirmed that the nature of crystal nucleation changes qualitatively in the vicinity of the metastable critical point. They also found that the nucleation barrier is significantly lower in this region than elsewhere in the phase diagram and that classical theory is invalid. Subsequently Sear studied a continuum model in which the structural order parameter was omitted.⁴ He carried out a mean field theory near the metastable critical point and showed that the liquid “tail” of the density profile of the critical droplet is described by an Ornstein–Zernike-type exponential behavior, whose range is given by the fluid correlation length. Since this length diverges as one approaches the critical point, so does the critical size of the droplet and the excess number of particles within it. In a subsequent paper Sear⁵ extended his arguments via a scaling theory using the critical exponents for the Ising universality class, so as to be valid in the vicinity of the critical point. In particular, the singular part of the free energy barrier associated with the tail was shown to satisfy the same scaling as the order parameter associated with the metastable critical point (the density difference) and vanishes as one approaches T_c . Sear did not calculate the shape of the droplet in the core and interface region and hence was unable to calculate the value of the barrier to nucleation.

In this paper we extend the work of Talanquer and Oxtoby, to obtain a better understanding of homogeneous crystal nucleation. We present additional numerical results for the model as well as an approximate analytical description of the critical droplet, including its crystal core and tail (the latter is based on Sear's work⁴). From this we compute the free-energy barrier to nucleation in the region between the fluid–

solid coexistence curve and the metastable fluid–fluid coexistence curve. As expected, this barrier is smallest in the vicinity of the metastable critical point. We show that classical nucleation theory is incorrect in the region between the liquidus and solid coexistence lines, except presumably very close to the liquidus line.

The outline of the paper is the following. In Sec. II we provide a brief review of the model. In Sec. III we extend the numerical analysis of Ref. 6 for the nucleation free energy barrier along various thermodynamic paths. We also calculate the profile of the critical droplet as a function of the density and structural order parameter. This yields the excess number of molecules, N , and the number of molecules in the crystalline phase, N_c , of the critical droplet. In the next section we present a brief discussion of the range of validity of classical nucleation theory and show that it is incorrect in the entire metastable region of the phase diagram that we explore. We also show results for the surface tension along different paths in the phase diagram. In Sec. V we present an approximate theory for the shape of the critical droplet and from this we obtain N and N_c . The theory accurately describes the critical droplet except in the interface region, and is in qualitative agreement with the numerical results for N/N_c . Section VI contains a brief conclusion. Some details of the numerical analysis are given in the Appendix.

II. MODEL

We use a model due to Talanquer and Oxtoby⁶ to describe globular protein crystallization. Their phase field model is based on the following grand canonical free-energy functional:

$$\Omega[\rho, m] = \int d\mathbf{r} [f(\rho, m) - \mu\rho + \frac{1}{2}K_\rho(\nabla\rho)^2 + \frac{1}{2}K_m\rho_s^2(\nabla m)^2]. \quad (1)$$

The free energy depends on two order parameters: the (conserved) local density $\rho(\mathbf{r}, t)$ and a (nonconserved) local structural order parameter that shows whether the system is in a solid or fluid phase $m(\mathbf{r}, t)$. Here $f(\rho, m)$ is the Helmholtz free-energy density and μ is the chemical potential. Talanquer and Oxtoby⁶ use the van der Waals free energy density for the fluid branch,

$$f_f(\rho, m) = k_B T \rho [\ln \rho - 1 - \ln(1 - \rho b)] - a \rho^2 + k_b T \alpha_1 m^2 \quad (2)$$

and a corresponding van der Waals free energy for the solid phase,

$$f_s(\rho, m) = k_B T \rho [\ln \rho - 1 - \ln(1 - \bar{\rho} b)] - (a + a_m m_s^2) \rho^2 + k_b T (\alpha_1 m^2 + \alpha_2). \quad (3)$$

Here $\bar{\rho}$ plays a role of a weighted coarse grained density $\bar{\rho} = \rho[1 - \alpha_3 m(2 - m)]$ where the term in square brackets implements a difference between the fluid and solid close-packing limits. For the fluid close-packing limit, $\rho b = 1$, while for the solid close-packing limit $\bar{\rho} b = 1$. The quantity $m_s(\rho)$ is the equilibrium value of the order parameter in the solid phase and hence is a solution of the equation

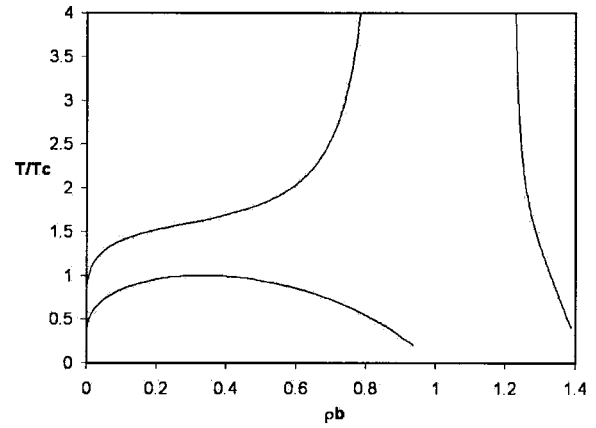


FIG. 1. Phase diagram for the particles with the short-range attraction interactions. The fluid–fluid coexistence curve becomes metastable in this case.

$(\partial f_s / \partial m)_{m_s(\rho)} = 0$. Thus in the solid close-packing limit ($b\bar{\rho} = 1$) $m_s = 1$. The parameter a_m in Eq. (3) has been introduced in order to change the range of the attractive interactions between molecules in the solid phase from that in the liquid phase [as described by the parameter a in equation (2)].

The chemical potential in the solid and fluid phases is the first derivative of the free energy with respect to density, $\mu = (\partial f / \partial \rho)_T$. In order to get coexisting densities ρ_α and ρ_β we must solve the equations $\mu(\rho_\alpha) = \mu(\rho_\beta)$ and $\omega(\rho_\alpha) = \omega(\rho_\beta)$, where $\omega = f - \mu\rho$. Graphically this gives the well-known “common tangent” rule for coexistence. By repeating this for different temperatures we can obtain the entire phase diagram.

In order to obtain a critical droplet profile we must solve the Euler–Lagrange equations with appropriate boundary conditions,

$$\frac{\delta\Omega}{\delta\rho} = 0 \quad \text{and} \quad \frac{\delta\Omega}{\delta m} = 0,$$

i.e.,

$$\begin{aligned} -K_\rho \nabla^2 \rho + \frac{\partial f}{\partial \rho} - \mu &= 0, \\ -K_m \nabla^2 m + \frac{\partial f}{\partial m} &= 0. \end{aligned} \quad (4)$$

Using the solutions of (4) for $\bar{\rho}(\mathbf{r})$ and $\bar{m}(\mathbf{r})$ we can obtain such properties of the inhomogeneous system as the free energy barrier $\Delta\Omega = \Omega\{\bar{\rho}(\mathbf{r}), \bar{m}(\mathbf{r})\} - \Omega\{\rho_0, 0\}$ and the surface tension $\sigma = 1/2(\int_0^\infty K_\rho |\nabla\rho|^2 dr + \int_0^\infty K_m |\nabla m|^2 dr)$.

III. NUMERICAL RESULTS

In the Appendix we describe the numerical methods that were used to solve Eqs. (4). Here we present some results, extending the work of Ref. 6, for the following choice of parameters: $a = 1$, $b = 1$, $\alpha_1 = 0.25$, $\alpha_2 = 2$, $\alpha_3 = 0.3$, $a_m = 1$. The phase diagram for these values is shown in Fig. 1, which shows in particular a metastable fluid–fluid coexistence

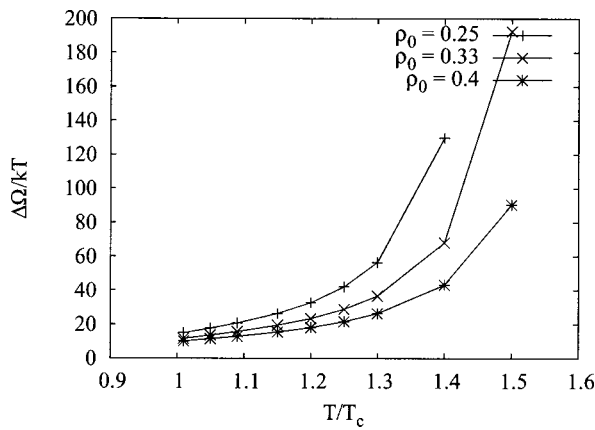


FIG. 2. Dependence of the free energy barrier versus temperature at constant density.

curve. The existence of the metastable critical point affects the nucleation and growth processes in the vicinity of this point.

The main quantity characterizing the nucleation process is a nucleation rate I , given by

$$I = I_0 e^{-\Delta\Omega/kT}, \quad (5)$$

where I_0 is a prefactor given by the product of dynamical and statistical parts.⁷ In order to understand how this metastable critical point affects nucleation, we calculate the free energy barrier for different thermodynamic paths. (Some results for this barrier were presented in Ref. 6.) The barrier dependence on temperature and density in the metastable region between the liquidus (solubility curve) and solidus lines is shown in Figs. 2 and 3. Figure 2 shows that as the temperature decreases, the barrier also decreases, while Fig. 3 shows that as the density increases, the barrier decreases. This is the normal behavior of a free energy barrier, since at any point on the solubility curve the free energy is infinite, decreases as one moves away from it, and vanishes at the solid coexistence curve.

However, the existence of the metastable fluid–fluid coexistence curve changes the pathways of the constant free energy barrier and constant supersaturation lines (Fig. 4) as compared with the case in which the critical point is not

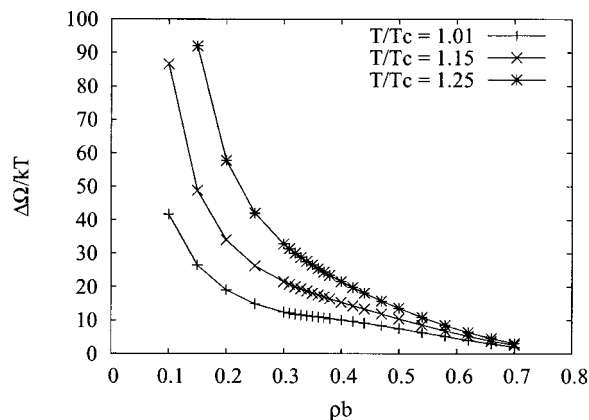


FIG. 3. Dependence of the free energy barrier versus density at constant temperature.

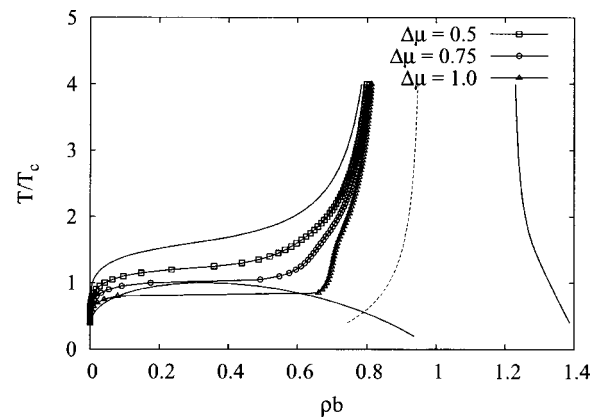


FIG. 4. The solid lines on the phase diagrams show the paths of constant supersaturation. The dashed line shows the border between the background fluid and background solid. If the background density is to the left of the dashed line, it corresponds to the fluid branch of the free energy. If it is to the right, it corresponds to the solid branch.

present. We can also see that along paths with constant supersaturation the free energy barrier decreases as one approaches the critical point (Fig. 5), which is consistent with Ref. 6. Figure 5 shows that the free energy barrier has a minimum near, but not at, the critical point. The location of this minimum changes from above the critical point for low supersaturation to below the critical point for high supersaturation. The free energy barrier increases below the critical point and becomes very sharp as one increases the supersaturation. When the constant supersaturation lines start to intersect the fluid–fluid coexistence curve, the free energy barrier becomes discontinuous at the temperature of intersection (Fig. 5 for $\Delta\mu = 0.8$ and $\Delta\mu = 0.9$.) In order to understand the behavior of the free energy barrier along the constant supersaturation lines, we first consider their shape (Fig. 4). At high temperatures these lines are more vertical (constant density lines) and the free energy barrier decreases with temperature, as shown in Fig. 2. Near the critical point the curves become almost horizontal (isothermal lines) and the barrier starts to increase (Fig. 3). Thus the shape of the constant supersaturation curve in some sense determines the be-

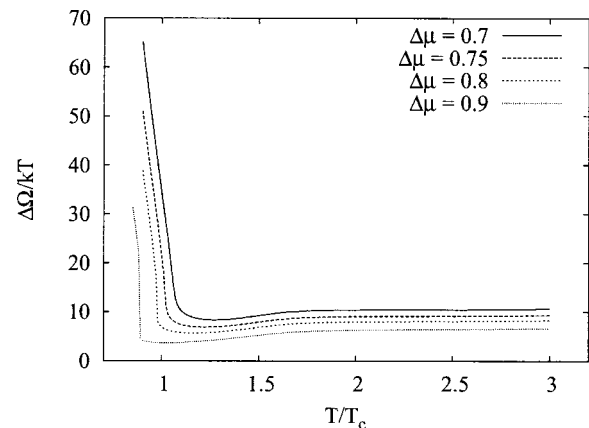


FIG. 5. Dependence of the free energy barrier versus temperature at constant supersaturation.

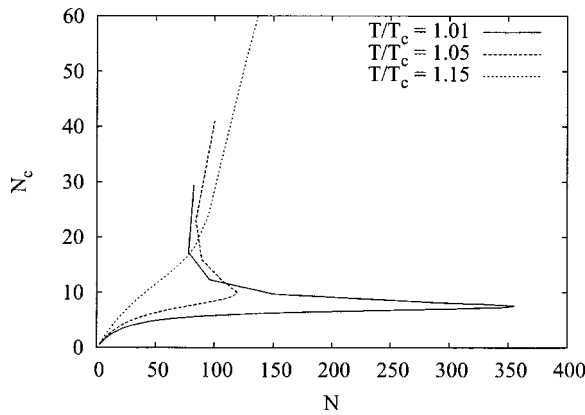


FIG. 6. The number of crystalline particles versus excess number of particles for different temperatures.

havior of the free energy barrier. To understand this in more detail, we note that the derivative of temperature with respect to density at constant supersaturation is

$$\left(\frac{\partial T}{\partial \rho_0}\right)_{\Delta\mu} = -\frac{\left(\frac{\partial \Delta\mu}{\partial \rho_0}\right)}{\left(\frac{\partial \Delta\mu}{\partial T}\right)} = -\left[\frac{f_{\rho\rho}^{(f)}}{\left(\frac{\partial \Delta\mu}{\partial T}\right)}\right]_{\rho=\rho_0}, \quad (6)$$

where $f_{\rho\rho}^{(f)}$ is evaluated at the background fluid density. This derivative vanishes at the critical point, so that the constant supersaturation lines become horizontal in the vicinity of the critical point. On the other hand, at large temperatures the denominator vanishes, so that the constant supersaturation lines become vertical. Thus we see that the presence of the critical point changes the behavior of the free energy barrier from decreasing as we lower the temperature far from the critical point (the vertical part of the $\Delta\mu = \text{const}$ lines) to increasing as we lower the temperature to its critical value (the horizontal part of the $\Delta\mu = \text{const}$ lines). Therefore somewhere in between there is a minimum of the free energy barrier. Thus we can conclude that the free energy barrier is relatively unaffected by the existence of the critical point along paths of constant temperature or constant density, whereas it plays a crucial role along paths of constant supersaturation.

One quantity of interest is the excess number of molecules, defined as the number of molecules in the presence of the droplet relative to the number of molecules in the spatially homogeneous metastable state,

$$N = \int_V (\rho(r) - \rho_0) d\vec{r}. \quad (7)$$

We can calculate the number of molecules in the crystalline state using $m(r)$, since this phase field shows whether a point is in the solid or fluid state. Thus,

$$N_c = \int_V m(r)(\rho(r) - \rho_0) d\vec{r}. \quad (8)$$

Mean field theory yields a divergence in the excess number of particles at the metastable critical point, whereas the number of particles in the crystalline state remains finite. Figure 6

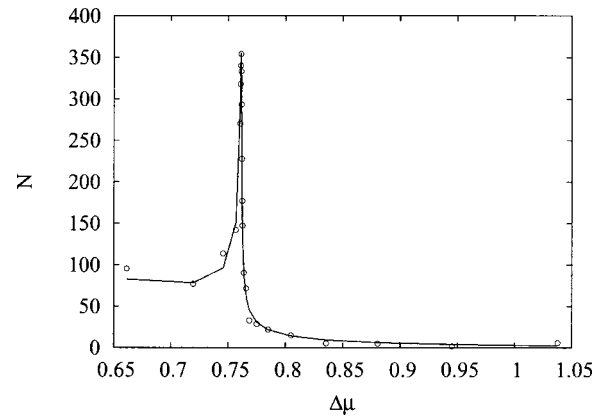


FIG. 7. The excess number of particles versus supersaturation (solid line). The circles are obtained by taking the derivatives of the free energy barrier with respect to the supersaturation.

shows N_c versus N for different supersaturations. We can check our numerical results with the nucleation theorem,^{8,9}

$$\frac{\partial \Delta\Omega}{\partial \Delta\mu} = -N. \quad (9)$$

Thus we can take a derivative of the free energy barrier with respect to supersaturation and compare this with our results for the dependence of the excess number of particles on the supersaturation (Fig. 7). We see that the free energy barrier decreases rapidly near the critical point as a function of the supersaturation. This happens because the background fluid density as a function of the supersaturation becomes flat in the vicinity of the critical point.

IV. BREAKDOWN OF CLASSICAL NUCLEATION THEORY

Classical nucleation theory (CNT) assumes that the critical droplet is large and that its interface is very sharp. It predicts that the free energy barrier is

$$\Delta\Omega_{\text{cl}} = \frac{16\pi\sigma^3}{3(\rho_s - \rho_0)^2 \Delta\mu^2}, \quad (10)$$

where $\Delta\mu$ is $\mu - \mu_{\text{coex}}$. However, classical nucleation theory becomes increasingly inaccurate as one approaches the metastable critical point.^{3,6} This is because the critical droplet has a diffuse interface in this region, in contradiction with the assumption of CNT. Our goal in this section is to compare CNT with our numerical results for the free energy barrier and to show that CNT has at best a very limited region of validity. It is useful to divide the contributions to the free energy barrier into two parts, i.e., the bulk and surface contributions, and compare our numerical results with the predictions of CNT for each of these separately. First, define

$$\Delta\Omega_{\text{bulk}} = 4\pi \int \Delta\omega(r) r^2 dr, \quad (11)$$

$$\Delta\Omega_{\sigma} = 4\pi \int \frac{1}{2} [K_{\rho} |\nabla\rho|^2 + K_m |\nabla m|^2] r^2 dr, \quad (12)$$

so the free energy barrier can be written as

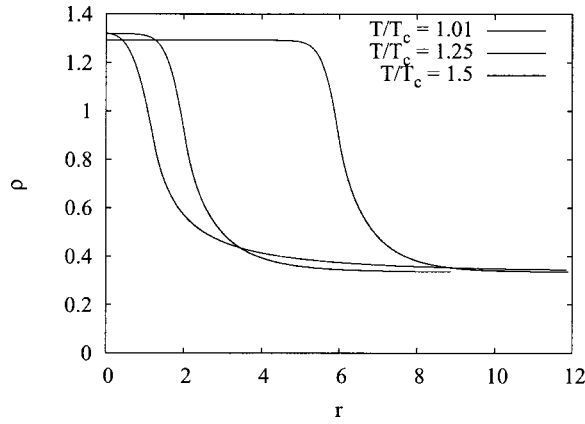


FIG. 8. Density profiles for different temperatures. From left to right, $T = 1.01$, $T = 1.25$, $T = 1.5$. The horizontal line shows the background fluid density.

$$\Delta\Omega = \Delta\Omega_{\text{bulk}} + \Delta\Omega_{\sigma}. \quad (13)$$

The classical approximation for this barrier is

$$\Delta\Omega_{\text{cl}} = \frac{4\pi R^3}{3} \Delta\omega_{\text{cl}} + 4\pi R^2 \sigma. \quad (14)$$

In the above, $\Delta\omega(r) = [f(\rho(r), m(r)) - \mu\rho(r)] - [f(\rho_0, 0) - \mu\rho_0]$ is the difference between the value of the grand canonical free energy at the points r and infinity, $\Delta\omega_{\text{cl}} = [f(\rho_s, m_s) - \mu\rho_s] - [f(\rho_0, 0) - \mu\rho_0]$ and σ is the surface tension. This division also allows us to determine which of these contributions to the free energy barrier is more important in the breakdown of CNT. We first note that if CNT is correct at some point (ρ, T) of the phase diagram, then the first terms of (13) and (14) should be equal; likewise, the second terms also should be equal. Therefore, the values of the radii that result from comparison of the first terms, i.e., $R_1 = (3\Delta\Omega_{\text{bulk}}/|\Delta\omega_{\text{cl}}|)^{1/3}$, as well as the second terms, $R_2 = (\Delta\Omega_{\sigma}/\sigma)^{1/2}$, should be equal to each other and to the classical radius of the droplet, $R_{\text{cl}} = 2\sigma/|\Delta\omega_{\text{cl}}|$.

Using this observation, we have checked the accuracy of CNT close to the liquidus line at low temperatures, as well as close to the critical point. The point close to the critical point is $T/T_c = 1.01$ and $\rho b = 0.33$, and those close to the liquidus line are $T/T_c = 1.5$, $\rho b = 0.33$ and $T/T_c = 1.4$, $\rho = 0.2$. For all these points CNT is incorrect. (For reasons described at the end of the Appendix we have been unable to explore the region very close to the liquidus line, where CNT presumably becomes correct.) Figure 8 shows the density profiles for these cases, while Table I shows the values of the corresponding quantities, $\Delta\Omega$, $\Delta\Omega_{\text{cl}}$, R_1 , R_2 , R_{cl} and the actual radius of the droplet R_a . We define the latter as the radius of a spherical droplet which has an infinitely sharp interface and

TABLE I. Values for comparison of our results with the classical nucleation theory. The points close to the critical point and liquidus line are $T/T_c = 1.01$ and $\rho b = 0.33$, and $T/T_c = 1.5$ and $\rho b = 0.33$, respectively.

	$\Delta\Omega$	$\Delta\Omega_{\text{cl}}$	R_1	R_2	R_{cl}	R_a
Close to liquidus line	100.7	12.3	3.83	6.11	3.15	6.53
Close to critical point	3.49	0.28	0.74	1.28	0.65	4.09

the same solid density and number of particles as our droplet. As can be seen from Table I, CNT underestimates the nucleation barrier by a factor of 10 as compared with the actual value for the model. It also underestimates the critical droplet size by a factor of 2. As one would expect, the ratio of the actual and classical nucleation barriers decreases as we approach the liquidus line. However, it is important to note that even in the region which is close to the liquidus line the difference between the actual and classical values of the barrier is still large. It seems, therefore, that CNT is accurate only very close to the liquidus line.

Since the interface of the droplet is not sufficiently sharp, the radius R_1 , and therefore the classical radius R_{cl} , is significantly different from the actual radius, R_a , of the droplet. This is responsible for the large difference between the classical and nonclassical values of the free energy barrier. The main contribution to the interface is its “tail,” which is given by the correlation length and hence becomes very large close to the critical point. At temperatures close to the critical temperature the system should be in the very narrow region near the fluid coexistence curve in order for the radius of the droplet to be much larger than the interface thickness, as given by the correlation length.¹⁰

V. THEORETICAL ANALYSIS

A. Approximations for the critical droplet

Equations (4) with appropriate boundary conditions define the saddle point of the free energy landscape in functional space. The boundary conditions are (a) that the density and structural order parameter at infinity are given by the metastable values and (b) their spatial derivatives are zero at the origin, i.e., $\rho(\infty) = \rho_0$, $m(\infty) = 0$, $d\rho/dr(0) = 0$, and $dm/dr(0) = 0$. There is a trivial, spatially uniform solution, satisfying these boundary conditions, given by $\rho(r) = \rho_0$, $m(r) = 0$. This uniform solution corresponds to the supercooled liquid, which is a metastable “point” in functional space. The critical droplet is a spatially inhomogeneous, unstable solution satisfying the same boundary conditions, which we find by first solving the Euler–Lagrange equations around the droplet core ($r = 0$). We assume that at the origin the density has a value close to ρ_s and the structural order parameter has a value close to m_s .¹¹ (In general the values of the density and structural order parameter at the droplet center are not equal to their equilibrium values, in contrast to the assumption of classical nucleation theory.) First, we represent the solution in the following form:

$$\rho(r) = \rho_s + \frac{\chi_\rho(r)}{r}, \quad (15)$$

$$m(r) = m_s + \frac{\chi_m(r)}{r}. \quad (16)$$

We substitute (15) and (16) into (4), rewrite these equations in terms of the χ 's and then linearize them to obtain

$$-K_\rho \frac{d^2 \chi_\rho}{dr^2} + f_{\rho\rho} \chi_\rho + f_{\rho m} \chi_m = 0, \quad (17)$$

$$-K_m \frac{d^2 \chi_m}{dr^2} + f_{m\rho} \chi_\rho + f_{mm} \chi_m = 0. \quad (18)$$

Here $f_{\rho\rho}$, $f_{\rho m}$, and f_m are the second derivatives of f at ρ_s and m_s . Because this is an approximation near the droplet core, we obviously cannot use the boundary conditions at infinity. So, in addition to the zero derivatives at $r=0$, we add two arbitrary boundary conditions at the origin. The boundary conditions for the χ 's therefore become the following: $\chi_\rho(0)=0$, $\chi_m(0)=0$, $\chi'_\rho(0)=\Delta\rho$, and $\chi'_m(0)=\Delta m$, where $\Delta\rho$ and Δm are the (unknown) shifts in the values of density and order parameter from ρ_s and m_s . The values of $\Delta\rho$ and Δm cannot be equal to zero, because in this case the solution is spatially uniform (see the Appendix). Solving Eqs. (17) and (18), we obtain

$$\chi_\rho = A \left(\frac{\sinh(q_2 r)}{q_2} - \frac{\sinh(q_1 r)}{q_1} \right) + \frac{\Delta\rho}{q_2^2 - q_1^2} \left(\frac{q_2^2}{q_1} \sinh(q_1 r) - \frac{q_1^2}{q_2} \sinh(q_2 r) \right) \quad (19)$$

and

$$\chi_m = B \left(\frac{\sinh(q_2 r)}{q_2} - \frac{\sinh(q_1 r)}{q_1} \right) + \frac{\Delta m}{q_2^2 - q_1^2} \times \left(\frac{q_2^2}{q_1} \sinh(q_1 r) - \frac{q_1^2}{q_2} \sinh(q_2 r) \right), \quad (20)$$

where

$$A = \frac{f_{\rho\rho} \Delta\rho + f_{\rho m} \Delta m}{K_\rho (q_2^2 - q_1^2)}, \quad B = \frac{f_{m\rho} \Delta\rho + f_{mm} \Delta m}{K_m (q_2^2 - q_1^2)},$$

$$q_{1,2}^2 = \frac{1}{2} \left[\left(\frac{f_{\rho\rho}}{K_\rho} + \frac{f_{mm}}{K_m} \right) \pm \sqrt{\left(\frac{f_{\rho\rho}}{K_\rho} - \frac{f_{mm}}{K_m} \right)^2 + \frac{4f_{\rho m}^2}{K_\rho K_m}} \right]. \quad (21)$$

Thus we obtain the solution at the center of the droplet in terms of two arbitrary parameters, $\Delta\rho$ and Δm . In principle these parameters could be obtained from the exact solution by matching this form to the boundary conditions at infinity.

Next we find the solution for the tail of the droplet.⁴ As $r \rightarrow \infty$ we have metastable boundary conditions, so we choose for the solution small deviations from the metastable values,

$$\rho(r) = \rho_0 + \frac{\delta_\rho}{r} e^{-q_\rho r},$$

$$m(r) = \frac{\delta_m}{r} e^{-q_m r}, \quad (22)$$

where δ_ρ and δ_m are arbitrary parameters and $q_\rho = 1/\xi_\rho^{(f)} = (K_\rho/f_{\rho\rho})^{1/2}$ and $q_m = 1/\xi_m^{(f)} = (K_m/f_{mm})^{1/2}$. The tail solution for m is in fact exact. We now have solutions in both the core and tail regions, but not in the interface region. Figure 9 shows the comparison of the numerically obtained density profile at $T/T_c = 1.2$ and $\rho_0 = 0.33$ with our approximations for the tail and the core. The tail approximation is rather good, but the core approximation becomes incorrect as one

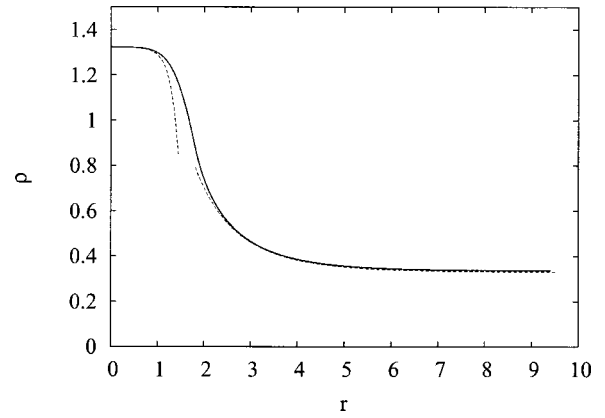


FIG. 9. Comparison of the numerically obtained density profile (at $T/T_c = 1.2$ and $\rho_0 = 0.33$) with the tail and core approximations (dashed lines).

approaches the interface region. For comparison purposes, we used the values of $\Delta\rho$, Δm , $\delta\rho$, and δm obtained numerically.

B. Approximation for N_c/N

N and N_c can each be considered as the sum of three terms: the number in the core, the tail and the interface. We can calculate the contributions to each of these from the core and tail, using the solutions for these two regions from the preceding section. Hence we can write

$$N^{(\text{core})} = \int_0^{R_{\text{core}}} \left(\rho_s + \frac{\chi_\rho(r)}{r} - \rho_0 \right) r^2 dr, \quad (23)$$

$$N^{(\text{tail})} = \int_{R_{\text{tail}}}^\infty \frac{\delta_\rho e^{-q_\rho r}}{r} r^2 dr, \quad (24)$$

where R_{core} is the maximum value of r for which we can still use the approximation near the center of the droplet, and R_{tail} is the minimum value of r for which the tail approximation can be considered as correct. The interface region is $R_{\text{core}} < r < R_{\text{tail}}$. In the core region, $\chi(r)/r \ll \rho_s$, so we can drop the second term in (23). Integrating (23) and (24) we find

$$N^{(\text{core})} = (\rho_s - \rho_0) V^{(\text{core})}, \quad (25)$$

$$N^{(\text{tail})} = \delta_\rho \xi_\rho^{(f)} (\xi_\rho^{(f)} + R_{\text{tail}}) e^{-R_{\text{tail}}/\xi_\rho^{(f)}}, \quad (26)$$

and similarly

$$N_c^{(\text{core})} = \int_0^{R_{\text{core}}} \left(m_s + \frac{\chi_m(r)}{r} \right) \left(\rho_s + \frac{\chi_\rho(r)}{r} - \rho_0 \right) r^2 dr, \quad (27)$$

$$N_c^{(\text{tail})} = \int_{R_{\text{tail}}}^\infty \frac{\delta_\rho e^{-q_\rho r}}{r} \frac{\delta_m e^{-q_m r}}{r} r^2 dr, \quad (28)$$

which gives us

$$N_c^{(\text{core})} = m_s (\rho_s - \rho_0) V^{(\text{core})}, \quad (29)$$

$$N_c^{(\text{tail})} = \delta_\rho \delta_m \frac{\xi_\rho^{(f)} \xi_m^{(f)}}{\xi_\rho^{(f)} + \xi_m^{(f)}} e^{-R_{\text{tail}}(1/\xi_\rho^{(f)} + 1/\xi_m^{(f)})}. \quad (30)$$

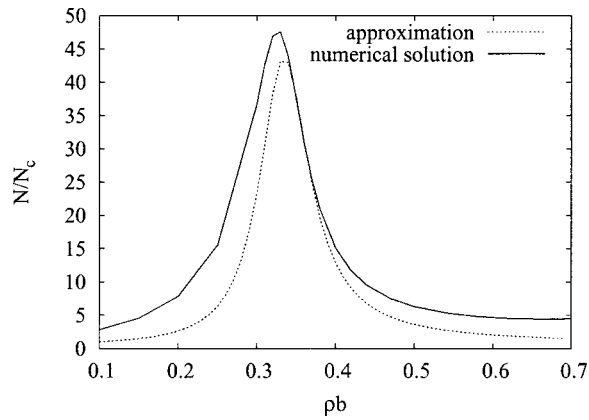


FIG. 10. Approximation for the ratio of the excess number of particles and the number of crystalline particles versus background density for $T/T_c = 1.01$, obtained by matching core solution directly with tail solution.

Next, we assume we can neglect contributions from the interface region, i.e.,

$$\frac{N_c^{(\text{core})} + N_c^{(\text{tail})}}{N^{(\text{core})} + N^{(\text{tail})}} \approx \frac{N_c}{N}. \quad (31)$$

In order to check this approximation, we compare its results with the numerical results. However, to do this we must discuss how we choose to determine the droplet profile, in order to estimate the ratio of N_c/N .¹²

We first note that the left-hand side of (31) depends on two parameters, R_{core} and R_{tail} (for simplicity we did not introduce different radii for ρ and m). R_{core} depends on the amplitudes $\Delta\rho$ and Δm , while R_{tail} depends on the amplitudes δ_ρ and δ_m . Therefore the left-hand side of (31) depends on four parameters. If we knew the interface solution analytically, we would be able to determine these four parameters by matching these solutions. As the approximation we could match the core and the tail solutions (so $R_{\text{core}} = R_{\text{tail}}$). This is the easiest to do but the least accurate. By setting $R_{\text{core}} = R_{\text{tail}} = R_{\text{match}}$ we must take into account that the core solution is obtained for the solid branch and the tail

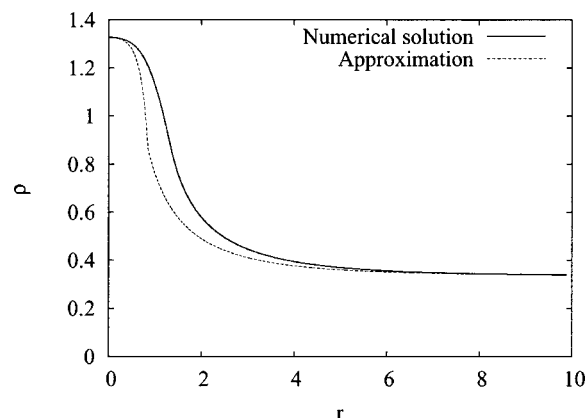


FIG. 11. Comparison of the numerically obtained density profile (at $T/T_c = 1.2$ and $\rho_0 = 0.33$) with the solution obtained by matching core solution (with parameters Δm and $\Delta\rho$ obtained numerically) with tail solution, without matching the derivatives.

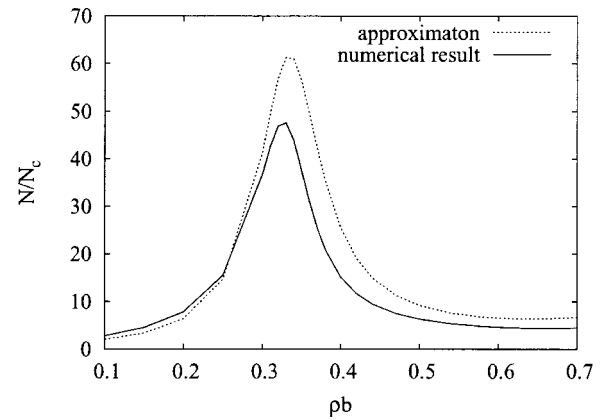


FIG. 12. Approximation for the ratio of the excess number of particles and the number of crystalline particles versus background density for $T/T_c = 1.01$ obtained by matching the core solution (with parameters Δm and $\Delta\rho$ obtained numerically) with the tail solution, without matching the derivatives.

solution is found for the fluid branch of the free energy. Therefore R_{match} is a point where the solid branch of the free energy intersects the fluid branch.

Figure 10 shows the dependence of the ratio of the excess number of particles and number of crystalline particles on the background densities for the case in which we match the core solution directly with the tail solution. As can be seen, this method gives the best estimate for this ratio near the critical point, since the tail plays a more important role in that region and the approximation for the tail of ρ is more accurate there. However, the actual values of N and N_c are each underestimated by a factor of 10.

As an alternative method we use the numerically determined $\Delta\rho$ and Δm to determine the core solution. Then we match the tail solution with this core solution at the point of intersection of the fluid and solid free energies. In this method the derivatives of ρ and m with respect to r are not equal at the fitting point (Fig. 11). As can be seen from Figs. 12 and 13 this approximation is qualitatively good close to

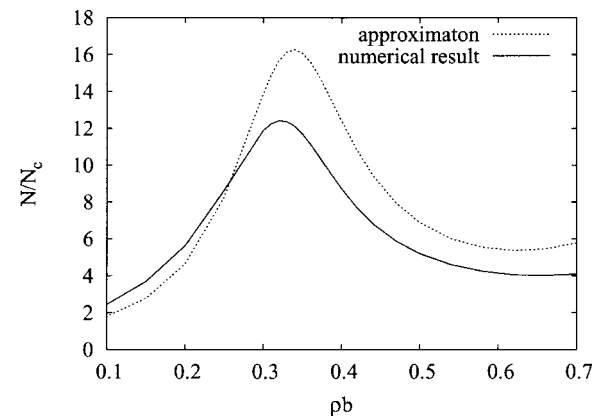


FIG. 13. Approximation for the ratio of the excess number of particles and the number of crystalline particles versus background density for $T/T_c = 1.05$ obtained by matching the core solution (with parameters Δm and $\Delta\rho$ obtained numerically) with the tail solution, without matching the derivatives.

the critical point, but becomes worse as T/T_c becomes larger. We still underestimate N and N_c , but not by as large a factor as in the above case.

However, close to the metastable critical point $N^{(\text{tail})}$ (and therefore N) diverges and becomes the leading term in the ratio (31), while N_c stays finite. Thus we can obtain the asymptotic behavior of the ratio (31) close to the metastable critical point. In this region we can rewrite (31) as

$$\frac{N_c}{N} \approx \frac{N_c}{N^{(\text{tail})}} \propto \frac{1}{(\xi_\rho^{(f)})^2} \propto f_{\rho\rho}^{(f)}. \quad (32)$$

Therefore close to the metastable critical point this ratio vanishes linearly with τ and quadratically with $\Delta\rho_c$,

$$\left(\frac{N_c}{N}\right)_{\text{metastable}} \propto \left(\tau + \frac{27}{8}(\Delta\rho_c)^2\right), \quad (33)$$

where $\tau = (T - T_c)/T_c$ and $\Delta\rho_c = \rho_0 - \rho_c$. Another asymptotic limit is the approach to the liquidus line. In this case the radius of the solid core diverges and therefore $N^{(\text{core})}$ and $N_c^{(\text{core})}$ become leading terms in (27) so at the liquidus line the ratio becomes

$$\left(\frac{N_c}{N}\right)_{\text{solubility}} = m_s. \quad (34)$$

We can see that there are two cases where the number of molecules in the critical droplet diverges, namely close to the critical point and close to the liquidus line, respectively. However, the number of molecules in the solid core of the droplet diverges only in the latter case. Thus close to the critical point most of the molecules are in the tail of the droplet, due to the divergence of the fluid correlation length, as first pointed out by Sear.⁴ At the liquidus line most of the molecules are in the solid core, whose radius diverges. Thus instead of one length scale (the radius of the droplet) we have two: the radius of the solid core and the fluid correlation length. The solid core of the globular protein crystal droplet can be observed experimentally,^{13,14} where it has been shown that close to the metastable critical point the core consists of only a few molecules (about 4–10). However, the existence of the long tail in the vicinity of the metastable critical point has not been directly observed.

VI. CONCLUSION

In this paper we have extended the numerical results⁶ to obtain a better understanding of nucleation for their model. In particular, we have calculated the density and structure order parameter profiles of the critical nucleating droplet for different temperatures. This solution of the saddle point equations then yields the free energy barrier to nucleation, which we have shown for a variety of different paths in the phase diagram. We also show in detail how classical nucleation theory is invalid everywhere in the region we studied, except presumably very close to the liquidus line. An approximate theory for the shape and properties of the critical droplet is developed that is in reasonable agreement with the numerical results, although there is clearly a need for a better description of the interface region that separates the core and tail of the droplet. Finally, we note that experiments show the

existence of a gel state for globular proteins, in part of the metastable region of the phase diagram.¹⁵ As a consequence, our discussion of the free energy barrier to nucleation for globular proteins would only apply to the region of the phase diagram in which there is no gelation, which is (roughly speaking) for densities $\rho \leq \rho_c$. The model studied here does not exhibit gelation.

ACKNOWLEDGMENTS

We wish to thank D. Oxtoby, V. Talanquer, and P. Vekilov for helpful discussions. This work was supported by a grant from the National Science Foundation, DMR-0302598.

APPENDIX: NUMERICAL SOLUTION OF SADDLE POINT EQUATIONS

Solving the equations (4) is a nonlinear two-boundary problem. One of the standard methods of solving this type of equation is the shooting method. Because it is very difficult to use the conditions at both boundaries simultaneously, we implement the boundary conditions on one side, and choose the number of free parameters equal to the number of boundary conditions on the other side. Then we can solve the resulting initial value problem. Depending on the final values (on the second boundary), we can decide how to change these free parameters. In our case we have two boundary conditions for $r=0$, which we can use directly, and two boundary conditions at $r=\infty$, which we cannot use directly. However, we can use $\Delta\rho$ and Δm as free parameters.

We still have several difficulties. First of all, the second boundary is at infinity, so we cannot explicitly get the values on this boundary. We could use some large finite value instead of infinity and avoid this problem, as long as the solution does not diverge at infinity for an incorrect choice of the parameters $\Delta\rho$ and Δm . Unfortunately it does diverge, so the linear shooting method does not work in this simple way. The reasons for the divergence are the error involved with the numerical method and the absence of solutions for most choices of $\Delta\rho$ and Δm . The error involved with the numerical method increases as we approach a cusp in free energy landscape; this is one of the reasons for the divergence. By varying the parameters $\Delta\rho$ and Δm we can push the beginning of this divergence to larger distances, so we can obtain part of the solution (including part of the tail) before the divergence occurs. However, this gives large errors in estimating such quantities as the free energy barrier, surface tension, etc. We could decrease the numerical error of the shooting method in the interface region by using Runge–Kutta methods with adaptive step size, but if we desire reasonably small values of the errors, the step size becomes too small for simulations.¹⁶

To avoid these difficulties we use a more advanced shooting technique—shooting with a fitting point. The fitting point was chosen at $r=R_{\text{core}}$ where the solid and fluid branches of the free energy intersect. The value of R_{core} depends on the parameters $\Delta\rho$ and Δm . Next, we know the exact solution for the fluid part of $m(r)$ (22), where δ_ρ is a parameter. By matching the fluid and solid parts of $m(r)$ and their derivatives at $r=R_{\text{core}}$ we determine Δm for fixed val-

ues of $\Delta\rho$ and $\delta\rho$. The next step is to obtain $\Delta\rho$ and $\delta\rho$ by matching the values and derivatives of the fluid and solid parts of $\rho(r)$. Note that the value of Δm depends on the value of $\Delta\rho$, so when we shoot with a particular value of $\Delta\rho$ we obtain a value for Δm each time. This shooting with a fitting point minimizes the numerical error as compared with standard shooting method.

There still is one remaining problem, even if we use shooting with a fitting point. Namely, as we approach the fluid coexistence curve, the values of $\Delta\rho$ and Δm become very small, so for shooting and fitting we need to vary them very slightly. Thus it becomes beyond the numerical limit of precision of the calculations to obtain a matching at the fitting point as we change these parameters. This so far prevented us from exploring the free energy barrier as one approaches the coexistence curve and hence we have not been able to determine where the classical theory becomes valid.

¹A. George and W. W. Wilson, *Acta Crystallogr., Sect. D: Biol. Crystallogr.* **D50**, 361 (1994).

²D. Rosenbaum, P. C. Zamora, and C. F. Zukoski, *Phys. Rev. Lett.* **76**, 150 (1996).

³P. R. ten Wolde and D. Frenkel, *Science* **277**, 1975 (1997).

⁴R. P. Sear, *J. Chem. Phys.* **114**, 3170 (2001).

⁵R. P. Sear, *J. Chem. Phys.* **116**, 2922 (2002).

⁶V. Talanquer and D. W. Oxtoby, *J. Chem. Phys.* **109**, 223 (1998).

⁷J. S. Langer, *Ann. Phys. (N.Y.)* **54**, 258 (1969).

⁸D. Kashchiev, *J. Chem. Phys.* **76**, 5098 (1982).

⁹Y. Viisanen, R. Strey, and H. Reiss, *J. Chem. Phys.* **99**, 4680 (1993).

¹⁰In our model the second derivative is not continuous, so we have a cusp in the maximum.

¹¹This is true unless the critical droplet becomes very small, which is the case for high supersaturations. We do not consider this case here.

¹²It is obvious that the accuracy of the approximation (31) depends on the accuracy of the core and tail solutions, as well as the relative contribution from the interface region. The maximum accuracy can be obtained by balancing between these two criteria. For example, if r_{core} is small, so the core solution is very accurate and r_{tail} is large, so the tail solution is also very accurate, then the gap between r_{core} and r_{tail} becomes large and therefore the interface region plays an important role and vice versa, if r_{core} is close to r_{tail} the interface region is not that important, but the accuracy of the core and tail solutions can decrease dramatically.

¹³O. Galkin and P. G. Vekilov, *J. Phys. Chem.* **103**, 10965 (1999).

¹⁴O. Galkin and P. G. Vekilov, *J. Am. Chem. Soc.* **122**, 156 (2000).

¹⁵P. G. Vekilov and A. A. Chernov, *The Physics of Protein Crystallization* (Academic, New York, 2002).

¹⁶This means that the step size Δr becomes so small that for the computer $1 + \Delta r$ becomes equal to 1. In our simulation Δr is about 10^{-15} .